

## Quantum Spin Hall effect in bilayer graphene heterostructures

Priya Tiwari, Saurabh Kumar Srivastav, Sujay Ray, Tanmoy Das and Aveek Bid\*

Department of Physics, Indian Institute of Science, Bangalore, India

### Abstract

Quantization of electrical conductance in condensed matter systems often arises from the presence of edge-modes<sup>1,2,3</sup>. These modes are globally protected from local perturbations by certain symmetries of the underlying system<sup>4,5</sup>. In the case of a time-reversal (TR) invariant 2-dimensional topological insulator (TI) – also known as the Quantum Spin Hall (QSH) insulator state<sup>6,7,8,9</sup> - the bulk of the system is gapped, while the edges host counter-propagating, gapless metallic conducting states of opposite spin polarizations<sup>7,8,9</sup>. Realizing TR invariant QSH in intrinsic graphene systems has been elusive so far due to the extremely weak spin-orbit interactions of carbon atoms. In this letter, we report the experimental observation of QSH state in bilayer graphene/single-layer WSe<sub>2</sub> heterostructures - a system similar to the one in which the pioneering proposals of Kane and Mele envisaged the QSH insulator state<sup>8</sup>. We find the measured value of electrical conductance to be quantized to the theoretically predicted value of  $e^2/h$  for each QSH edge-mode. The linear conductance obtained in several measurement configurations matches precisely with that obtained from a tight-binding model replicating our heterostructure with periodic [for bulk topology] and open-boundary conditions [for topological edge-modes]. Our work provides the pivotal affirmation of the archival Kane-Mele model for QSH state in graphene and expands the material choices for QSH states.

### Main

Topological phases of quantum many-body systems are characterized by global topological properties that emerge from symmetry protected, local degrees of freedom. They play a pivotal role in the study of electronic states like the Quantum Hall phase, which does not break any symmetries but has a set of distinct properties that cannot be changed via local perturbations without going through a quantum phase transition<sup>4,5</sup>. In essence, they are characterized by a bulk state which is topologically distinct from the vacuum and which has a finite quasiparticle energy gap: this leads to the appearance of dissipationless, quasi-one-dimensional edge-modes. A spinful system of electrons in two-dimensions has four-degrees of freedom - two spin species and two directions of momentum. In the QSH insulator phase, these four modes get separated in a TR invariant way to give rise to an insulating bulk and quantized, helical edge-modes (which form a Kramer's doublet) that are topologically protected from scattering<sup>7</sup>.

[\\*aveek@iisc.ac.in](mailto:aveek@iisc.ac.in)

The seminal proposal by Kane and Mele<sup>7,8</sup>, which acted as a precursor to topological insulators (TI), envisaged creating a QSH phase by coupling the orbital and (pseudo-)spin degrees of freedom in single-layer graphene. In this model, the separation between the helical edge states arises physically from the TR invariant spin-orbit coupling. The spin- $\uparrow$  and spin- $\downarrow$  charge-carriers experience opposite forces due to spin-orbit interaction (SOI) and hence form edge-modes of opposite chirality<sup>9</sup>. Due to extremely weak spin-orbit coupling in graphene, experimental verification of the Kane-Mele model has been challenging to realize. There have been several attempts to increase the spin-orbit interaction in graphene by either decorating it with heavy atoms<sup>10</sup> or by doping it with topological nanoparticles<sup>11</sup>. These methods, although providing signatures of the spin-Hall effect, were found to drastically degrade the mobility of the graphene.

An alternative, non-invasive, method is to 'induce' strong spin-orbit coupling in graphene by proximity to an appropriate high SOI material<sup>12</sup>. Several studies, both theoretical and experimental, have demonstrated that a large SOI can be induced in graphene in proximity to few-layer transition metal dichalcogenides (TMD) like  $WS_2$  or  $WSe_2$ <sup>13</sup>. Recently, it has been predicted that graphene on  $WSe_2$ , under certain conditions, can have an inverted band structure<sup>14</sup>. The system can thus host topologically protected helical edge states and is, therefore, a promising platform to study the QSH effect. Although the QSH effect has been observed in other semiconductor devices<sup>15,16,17,18,19,20</sup>, confirmation of the TR invariant Kane-Mele model in graphene is lacking.

In this letter, we report the first observation of robust TR invariant QSH state in bilayer graphene (BLG). Strong SOI was induced in the BLG by proximity to single-layer  $WSe_2$ . The measured conductance in several multi-probe measurement configurations (both local and non-local) was found to be precisely quantized over a range of temperatures (20 mK- 10 K); the quantized value in all cases being equal to that expected for helical edge structure of QSH phase. We also find the measured non-local resistance to scale linearly with the longitudinal resistance, which firmly establishes that the electrical transport in our system proceeds via edge-states.

## **Experimental details**

Hall bar devices based on an atomically sharp interface between bilayer graphene and a monolayer of semiconducting crystalline  $WSe_2$  were fabricated using standard dry transfer technique<sup>21</sup> - the BLG/ $WSe_2$  being encapsulated between hexagonal boron nitride (hBN)

crystals (Figure 1(a)). The hBN layers acted as gate dielectrics for the top and bottom gates. Electrical contacts were achieved by reactive dry ion etching and thermal deposition of Cr/Au (for details see Supplementary text 1: Device Fabrication and characterization). Figure 1(b) is the Raman spectra of the BLG/WSe<sub>2</sub> stack. The presence of a peak near 250 cm<sup>-1</sup> (and the absence of one at around 308 cm<sup>-1</sup>)<sup>22</sup> confirmed the WSe<sub>2</sub> flake to be a monolayer. The other two Raman, peaks centred around 1580 cm<sup>-1</sup> (G peak) and 2800 cm<sup>-1</sup> (2D peak), belong to the graphene layer. The spectral decomposition of the 2D peak (see Figure S5(b)), as well as the intensity ratio of G and 2D peaks, establish the graphene to be a bilayer<sup>23</sup>. The room temperature photoluminescence spectra of the WSe<sub>2</sub> flake (Figure 1(c)) has a peak at ~1.65 eV, confirming that it is a monolayer<sup>24</sup>.

All electrical measurements were performed in a cryogen-free dilution refrigerator at a base temperature of 20 mK using standard low-frequency lock-in techniques with excitation currents of 1 nA. The dual-gate architecture of the device allowed independent tuning of both the charge-carrier number density,  $n$ , and the displacement field perpendicular to the device,  $D$ . A logarithmic scale contour plot of the 4-probe longitudinal resistance as functions of the back-gate voltage,  $V_{bg}$  and the top-gate voltage,  $V_{tg}$  (Figure 1(d)) shows that the resistance at the primary Dirac point (PDP) increases with an increase in  $|D|$  establishing the opening of a bandgap in BLG. Along with the prominent peak at the primary Dirac point (PDP), there are two other satellite peaks symmetrically placed around  $n = 0$ . These two satellite peaks, called clone Dirac points (CDP), are the result of band structure reconstruction of BLG due to the Moiré super-lattice potential, which is a long-wavelength, weak periodic potential caused by a near-perfect alignment of the top hBN layer with the top layer of the BLG<sup>25,26,27,28</sup>. From the positions of the CDP, the angle between top hBN and the BLG was found to be  $\sim 0.9^\circ$  (Supplementary text 2: Hofstadter's butterfly and Moiré superlattice)<sup>26,29,30,31,32</sup>. In Figure 1(e) is plotted the 2-probe resistance measured across the device versus the charge-carrier density  $n$  and the displacement field  $D$ . The asymmetric feature seen near the PDP (outlined by dashed lines) is a consequence of the fact that depending on the direction of  $D$ , the band-splitting in the BLG by the induced SOI<sup>33</sup> occurs either in the conduction band or in the valence band (see Supplementary text 5: Calculations of edge and bulk dispersion relations).

### **Spin-orbit interaction in BLG**

In a system with SOI, long-range spin currents can be generated by the spin Hall effect (SHE)<sup>34,35,36,37</sup> which produce a nonlocal signal at voltage probes remote from the charge current path via the inverse SHE. The zero magnetic (B)-field nonlocal resistance  $R_{NL}$  is peaked sharply near the primary Dirac point (Figure 2(a)). At large  $|D|$ ,  $R_{NL}$  has a split peak

(Figure 2(b)). Recall that the strength of the Berry curvature is most significant at the band-edges, at the so-called ‘Berry curvature hot-spots.’ This causes the effect of the SHE to be most prominent when the chemical potential of the system lies at the band-edges<sup>38</sup>. With an increasing magnitude of  $|D|$ , the magnitude of bandgap in BLG increases causing the Berry curvature hot-spots in the valence- and conduction-bands to move apart – this can be mapped out in our system by monitoring the location of the peak of  $R_{NL}$  in the  $n - D$  plane.

A plot of the transverse resistance measured at finite values of  $|n|$  (when the chemical potential is inside the bulk valence band and at  $B = 0$ ) is shown in Figure 2(c). One finds a large  $R_{xy}$  arising from the SHE. The observation of a large  $R_{NL}$  at band-edges, zero magnetic field  $R_{xy}$  inside the bulk band ( (a)), SOI induced splitting of the band-edges seen from SdH oscillations (Figure S6), weak anti-localization correction to the low-field magnetoresistance (Figure S8; Supplementary text 3: Effect of the SOI induced by WSe2 in BLG) and the asymmetry in the plot of  $R(B = 0)$  (Figure 1(e)) all confirm that the induced SOI is considerably strong in the BLG.

### **Quantized transport through edge-modes**

The observed significant increment in the strength of the spin-orbit interaction of the BLG heterostructure leads to the expectation that it will host the QSH phase (see Supplementary text 5: Calculations of edge and bulk dispersion relations). The plots of the measured 4-probe and 2-probe longitudinal resistances for  $B = 0$  and  $T = 8$  K shown in Figure 3 establish that this indeed is the case. Figure 3(a) shows precise quantization of the 4-probe longitudinal resistance to  $h/(2e^2)$  at the primary Dirac point over a range of applied electric fields. In Figure 3(b) is plotted the measured 2-probe resistance which quantizes to  $3h/(2e^2)$ . These two values are exactly what one would expect from the given contact configuration for helical edge-modes (Supplementary text 4: Extended data and Landauer Büttiker formalism). The quantization of the 2-probe and 4-probe longitudinal resistances at the PDP over a range of values of the displacement field is the central result of this letter and establishes the presence of helical edge modes in our device. Figure 3(c) and Figure 3(d) are respectively the plots of the 4-probe, and 2-probe longitudinal resistance plotted versus  $n$  and  $|D|$ . The data projected on the  $n - R$  plane shows that the quantization in each case is centred around the primary Dirac point (with  $\Delta n = \pm 2 \times 10^{-11} \text{ cm}^{-2}$ ).

It may be argued that the observed quantization of the 4-probe longitudinal resistance can be due to the ballistic nature of the short-channel device or a fortuitous arrangement of scatterers. To address the first issue, the longitudinal resistance of the device was measured in several

multi-terminal configurations. The data for two such configurations are shown in Figure 4, along with the respective measurement configurations (results for two more configurations are presented in Supplementary text 4: Extended data and Landauer Büttiker formalism). The grey lines are the values of longitudinal resistance calculated for the helical QSH edge-modes using the Landauer-Büttiker formalism for quantum transport in multi-terminal devices. Note that, for chiral edge-modes, the expected values of the resistance for the configuration in Figure 4(a) is zero, and for that in Figure 4(b) is  $h/e^2$ . The excellent match between the measured resistance and the predictions based on helical edge-modes establishes again that the system is indeed in the QSH phase near the primary Dirac point. The second objection can be ruled out by noting that almost identical data were obtained over several thermal cycles of the device from room temperature to 20 mK (comparison of results from two cool-downs are presented in Figure S7).

The  $R_{NL}$  signal was measured as a function of the magnetic field,  $B$  applied perpendicular to the plane of the device. As  $B$ -field breaks TR symmetry, it should lead to a quenching of the QSH state and consequent decay of the non-local signal. However, the non-local signal can persist as long as  $2\Delta > 2E_Z$ , where  $\Delta$  is the energy-gap for the QSH state and  $E_Z$  is the Zeeman energy<sup>39</sup>. From the temperature dependence of the quantized conductance,  $\Delta$  was estimated to be about 7 meV. This yields the maximum magnetic field range till which the quantization can persist to be  $B_{\max} \sim \Delta^2 / (m\mu_B v_F^2) = 0.1$  T, which matches very well with our observations (see Supplementary text 6: Presence of non-local signal and edge transport). Here  $m$  is the free-electron mass,  $\mu_B$  is the Bohr magneton and  $v_F \sim 1.2 \times 10^6$  ms<sup>-1</sup> the Fermi velocity.

The measured quantization in longitudinal resistance in several different configurations (Figure 3, Figure 4, and in Supplementary text 4: Extended data and Landauer Büttiker formalism) and the presence of a sizeable non-local signal at the primary Dirac point firmly establishes that the charge-carriers in this device are propagating via edge-modes.

### Theoretical calculations

To get a quantitative estimate of the band structure, we construct a tight-binding model with SOI for the AB-stacked (Bernal stacking) BLG on WSe<sub>2</sub> heterostructure, as used in our experimental investigations (for details see SI). Due to the difference in the electric polarization between the two layers for an applied electric field  $|D| \neq 0$ , the layer degeneracy in BLG is lifted, and a bandgap opens at the Fermi level. This leads to the localization of carriers in conduction and valence band bands in different layers of the BLG. The induced SOI is significant only for the band that accommodates the carriers localized in the layer closer to the single-layer WSe<sub>2</sub>. Hence in the corresponding band, the energy levels for the  $\uparrow$  and  $\downarrow$  spins

split as seen in Figure S10 for  $D = 0.2 \times 10^9$  V/m and  $D = -0.2 \times 10^9$ . It is instructive to note that as one moves from negative to positive  $D$ , this band undergoes inversion and topological phase transition. For the other band, the splitting due to SOI is negligible.

Next, we calculated the edge-modes with open boundary conditions in one direction - a zigzag edge on the boundary (see Supplementary text 5: Calculations of edge and bulk dispersion relations). For  $D = 0$ , the dispersions of the edge-modes are extremely flat at the Fermi level with  $v_F \sim 0$  - these modes thus carry negligible current (Figure 4(e)). With increasing  $|D|$ , the bulk becomes gapped, and dispersive edge states appear (Figure 4(d) and (f)). Each edge of the device now supports two such counter-propagating modes - one each for the up and the down spins. Thus, our calculations confirm the emergence of helical edge-modes of the QSH state in BLG with strong SOI (see Figure S10 in SI for detailed plots of band structure and density of states).

Note that the bulk bandgap for BLG at  $|D| = 0.2 \times 10^9$  V/m is around  $50 \text{ meV}^{40}$ , which is much larger than the relevant energy scales in the problem - temperature (which ranges from 20 mK-10 K), the energy-scale over which the edge states evolve ( $\sim 1 \text{ meV}$ ) and  $\Delta$ , the energy gap for the QSH state. This ensures that when the chemical potential is near the PDP at large  $|D|$  there is no contribution from the bulk of the BLG to electrical transport in the system.

## Discussions

The presence of hBN aligned with the top layer of the BLG (with the consequent Moiré superlattice potential) suggests that the observed  $R_{NL}$  may also plausibly arise either from the Valley Hall (VH) or the Quantum Valley Hall (QVH) effect. The first scenario can be ruled out by noting that in the case of VH, transport proceeds through the bulk of the material resulting in the non-local resistance  $R_{NL}$  scaling as  $\rho^3$ , where  $\rho$  is the local 4-probe longitudinal resistivity. Figure 4(c) shows that in our device scales linearly with  $\rho$ , where  $\rho$  is the local 4-probe longitudinal resistivity, establishing again that transport is confined to the edges of the device<sup>41,42</sup>. Figure 4(c) shows that in our device scales linearly with  $\rho$ , establishing again that transport is confined to the edges of the device.

In the case of the QVH effect<sup>43</sup>, the quantization in the measured resistance at zero magnetic fields has been observed primarily near the CDP, not the PDP<sup>39</sup>. On the contrary, the quantization results presented in this letter were all obtained at the PDP. Measurements of  $R_{NL}$  in the presence of a perpendicular magnetic field shows that for  $B < B_{max}$ , the non-local signal also appears only near the PDP (see Supplementary text 6: Presence of non-local

signal and edge transport). These, and the fact that the 4-probe conductance quantization observed in our device was  $2e^2/h$ ; and not  $4e^2/h$  as should be the case for QVH for BLG (two modes originating from spin-degeneracy and two from layer quantum number) effectively rule out QVH as the origin of our observations.

In summary, the experiments presented in this letter unambiguously demonstrate the QSH insulator phase in bilayer graphene/ single-layer WSe<sub>2</sub> heterostructure. Our approach demonstrates magnetic field independent edge-state transport in an ultra-high mobility material system. It provides a novel and accessible platform to controllably perform measurements of spin-transport in two-dimensional systems in geometries analogous to those employed in quantum optics. It thus opens a new paradigm for utilizing the pseudospin degree of freedom in graphene for various pseudo-spintronics<sup>44</sup> and quantum computation applications<sup>45</sup>, including quantum information and quantum processing.

### **Acknowledgments**

The authors acknowledge fruitful discussions with Anindya Das, Atindra Nath Pal, and Hemanta Kumar Kundu. The authors acknowledge device fabrication facilities in NNFC, CeNSE, IISc. S.K.S. acknowledges PMRF, MHRD, for financial support. A.B acknowledges funding from SERB, DST, and IISc for financial assistance.

### **Contributions**

P.T. fabricated the devices; P.T., S.K.S. and A.B. performed the measurements; S.R. and T.D. provided theoretical support. P.T., S.K.S. and A.B. designed the study and performed the analysis. P.T., S.K.S. and A.B. co-wrote the manuscript. All authors discussed the results and commented on the manuscript.

### **Corresponding author**

Correspondence to [Aveek Bid](#)

### **Competing interests**

The authors declare no competing interests.

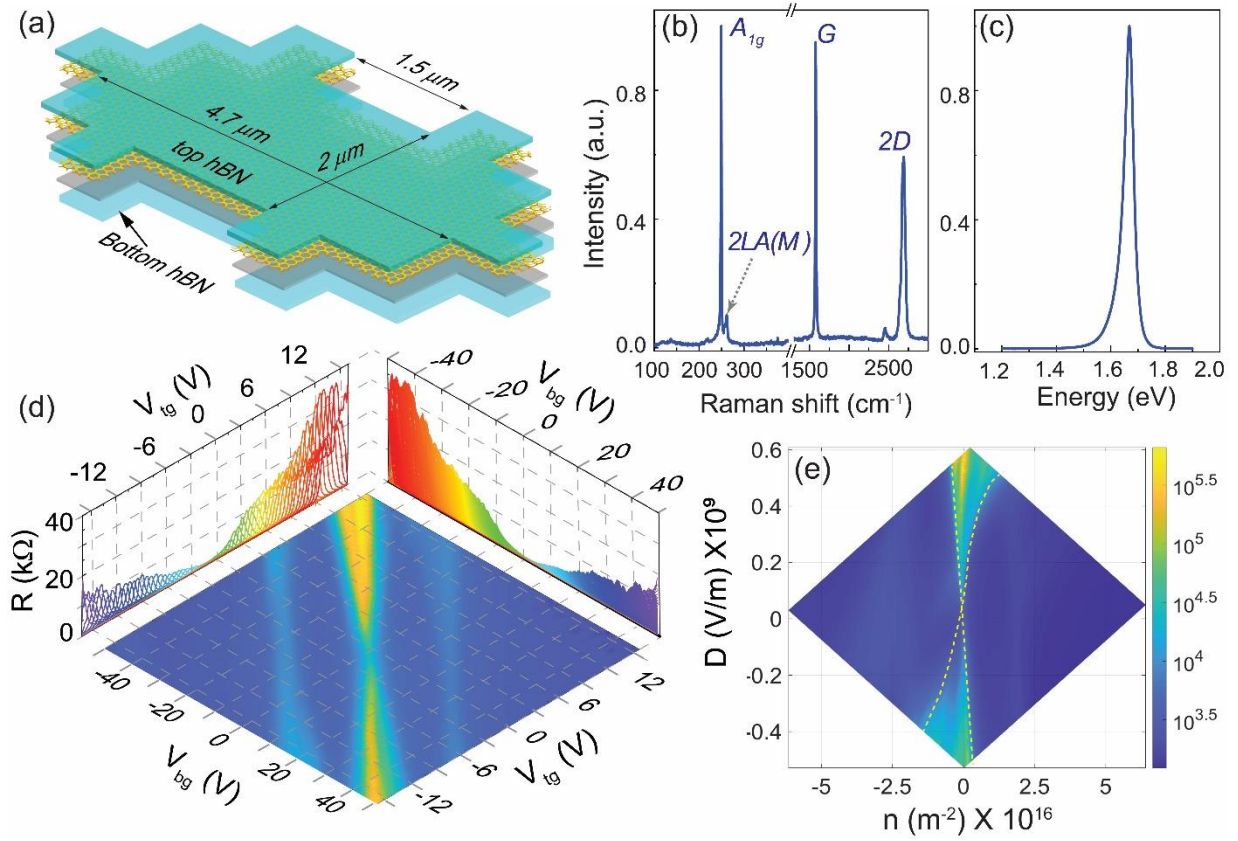


**Figure 1: Device structure and characterization.** (a) A schematic of the device configuration. The co-laminated heterostructure of BLG (shown as honeycombed structure) and single-layer WSe<sub>2</sub> (grey layer) is sandwiched between two hBN flakes, each of thickness  $\sim 20$  nm. (b) Room temperature Raman spectra of the WSe<sub>2</sub> and BLG flakes. The peaks corresponding to single-layer WSe<sub>2</sub> and BLG are marked. (c) Room temperature photoluminescence response of WSe<sub>2</sub> flake – the peak at 1.65 eV establishes it to be a monolayer. (d) Contour plot of the 4-probe longitudinal resistance as a function of the  $V_{bg}$  and  $V_{tg}$ . The panel on the right shows the projection of the data on  $R - V_{bg}$  plane, while the left-panel shows the projection of the data on the  $R - V_{tg}$  plane. The data presented in this figure were acquired at  $T = 20$  mK and  $B = 0$  T. (e) Logarithmic scale color plot of the 2-probe longitudinal resistance versus the displacement field  $|D|$  and the net charge carrier concentration,  $n$ . The asymmetry around the primary Dirac point (region marked by the dashed line) is a consequence of the fact that only one of the bands (either valence-band or conduction-band, depending on the direction of  $D$ ) get split due to induced SOI. The data presented in this figure were acquired at  $T = 8$  K and  $B = 0$  T.

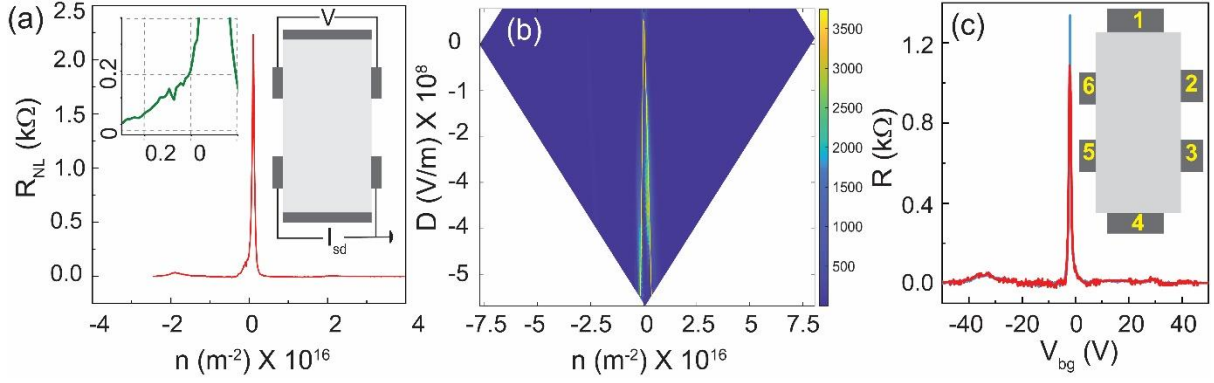


Figure 2: **Non-local resistance and SHE.** (a) Measured non-local resistance,  $R_{NL}$  plotted versus  $n$  for  $D = 1.2 \times 10^8$  V/m. Left inset: zoom-in of  $R_{NL}$  near the PDP. Right inset: schematic of the measurement configuration. (b) Contour plot of  $R_{NL}$  as a function of  $n$  and  $D$ . The yellow dotted lines highlight the splitting observed in the  $R_{NL}$  peak at large  $|D|$ . (c) A plot of  $R_{xy}$  measured at  $B = 0$ . For the data plotted in solid blue line, the current is sourced between contacts 1 and 4 while the voltage drop is measured between contacts 6 and 2. For the data plotted in solid red line, the current and voltage contacts are interchanged. The  $R_{xy}$  arises from SHE (for details see main text). The data were collected at  $B = 0$  and  $T = 20$  mK.

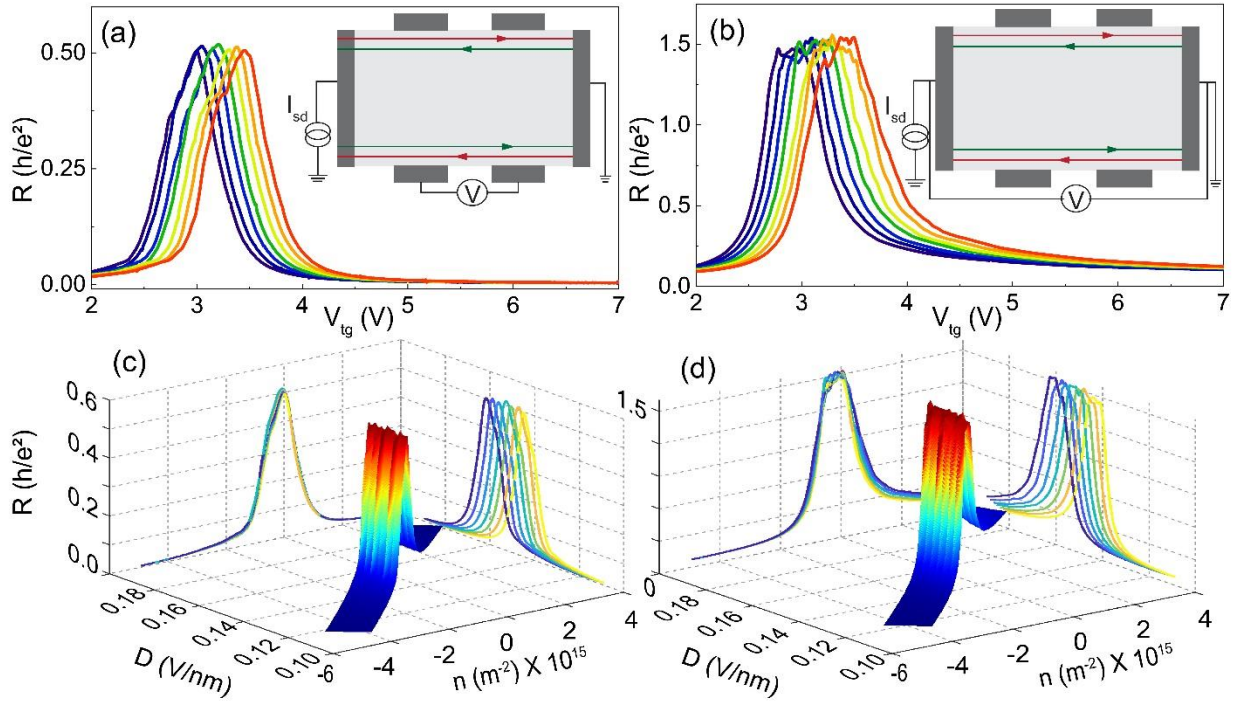


Figure 3: **Quantization of longitudinal resistance at  $B = 0$ .** (a) Quantization of the 4-probe resistance to  $h/(2e^2)$  at several values of  $V_{tg}$  (keeping  $V_{bg}$  fixed) such that the fermi level lies in the bulk bandgap. The inset is a schematic of the 4-probe measurement configuration - the red and green lines represent the spin-filtered edge-modes. (b) Quantization of the 2-probe resistance to  $3h/(2e^2)$ , the data were acquired simultaneously with the data presented in (a). The inset is a schematic of the 2-probe measurement configuration (c) Plot of 4-probe  $R$  versus  $n$  and  $|D|$ . The projection on the  $R - n$  plane shows that the quantization is around  $n = 0$ , while the projection on the  $R - D$  shows the quantization over a range of values of the displacement field. (d) A plot of 2-probe  $R$  versus  $n$  and  $|D|$ . The projection on the  $R - n$  plane again shows that the quantization is around the PDP. All the data were acquired at  $T = 8$  K and  $B = 0$  T (quantization obtained at 20 mK and for other cool-downs are presented in the SI).

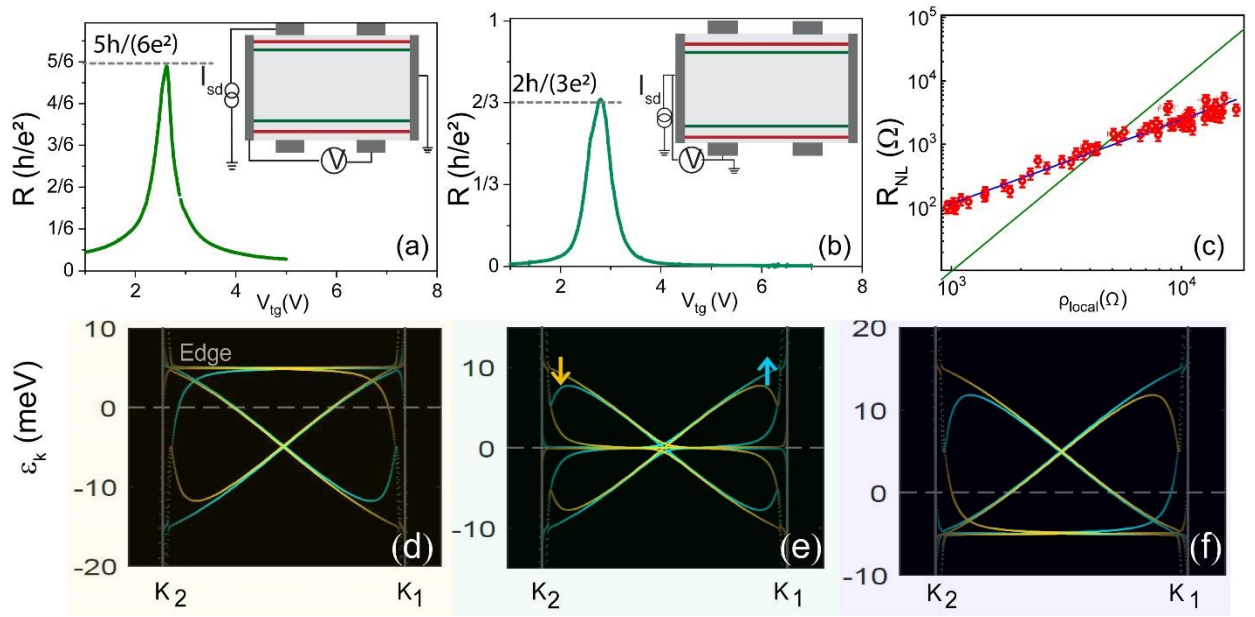


Figure 4: **Quantization of longitudinal resistance at different multi-probe measurement configurations.** (a) Quantization of  $R$  to  $2h/(3e^2)$  in a 3-probe measurement geometry – the corresponding measurement configuration is sketched in the inset. Note that for chiral edge states, in this configuration,  $R$  would equal zero. (b) Quantization of  $R$  to  $5h/(6e^2)$  – the corresponding measurement configuration is shown in the inset. For this measurement configuration, chiral edge states would yield  $R = h/e^2$ . (c) Plot of  $R_{NL}$  versus the local longitudinal resistivity  $\rho_{local}$  measured at  $D = -1.2 \times 10^8$  V/m. The filled red circles are the measured data points, the solid blue line is a fit to  $R_{NL} \propto \rho_L$ . The solid green line represents a plot of  $R_{NL} \propto \rho_L^3$ . The linear dependence of the non-local resistance on the local resistivity indicates that edge-transport dominates in the system. The lower panel shows the calculated spin splitting of the edge-modes for (d)  $D = -0.2 \times 10^9$  V/m, (e)  $D = 0$  V/m, and (f)  $D = 0.2 \times 10^9$  V/m.

## Methods and extended data

Methods and extended data .....	12
Supplementary text 1: Device Fabrication and characterization.....	12
Device fabrication .....	12
Supplementary text 2: Hofstadter's butterfly and Moire superlattice.....	13
Supplementary text 3: Effect of the SOI induced by WSe <sub>2</sub> in BLG .....	14
Determination of splitting in Fermi surface from SdH oscillations.....	14
Weak anti-localization in BLG .....	14
Supplementary text 4: Extended data and Landauer Buttiker formalism.....	15
Reproducibility of the 2-probe and 4-probe quantization data .....	15
Measurements in multi-terminal configurations.....	15
Supplementary text 5: Calculations of edge and bulk dispersion relations.....	18
Supplementary text 6: Presence of non-local signal and edge transport.....	20
Ohmic contribution to non-local signal: .....	20
B-field dependence of <b>RNL</b> : .....	21

### Supplementary text 1: Device Fabrication and characterization

#### Device fabrication

Graphene WSe<sub>2</sub> heterostructure encapsulated with hBN flakes were fabricated following a standard dry transfer technique<sup>46,47,48</sup>. Flakes of hBN (~15-40nm), bilayer graphene (BLG), and single-layer WSe<sub>2</sub> (SL-WSe<sub>2</sub>) were mechanically exfoliated on SiO<sub>2</sub>/Si wafers. BLG was identified from Raman spectroscopy, while and the thickness of the WSe<sub>2</sub> was determined using both Raman spectroscopy and photoluminescence, as described in the main text. The 2D-peak of graphene could be spectrally decomposed into four Lorentzians<sup>23</sup> with peak frequencies 2639, 2675, 2693, and 2709 cm<sup>-1</sup> as shown in Figure S5(c). All the flakes - hBN, BLG, and WSe<sub>2</sub> were staked using the "hot pick-up" technique<sup>21</sup>. The transfers were done in a customized home-built transfer set-up based on a mechanically controllable XYZ stage using a long working distance 50X-objective under an optical microscope.

To assemble the flakes in the desired sequence, Polydimethylsiloxane (PDMS) was coated with PolyBisphenol A Carbonate (PC) and mounted on the glass slide clamped to the micromanipulator. The exfoliated hBN was first picked on PC at 90° C, then BLG was picked up by hBN 90°C with its edge aligned with that of the hBN to achieve Moire superlattice. This

was followed by sequential pick up of SL-WSe<sub>2</sub> and hBN. Next, the full assembled stack was then transferred on to SiO<sub>2</sub>/Si<sup>++</sup> wafer at 180°C. The stack was cleaned in chloroform (CHCl<sub>3</sub>) followed by acetone and isopropylalcohol (IPA) for removing PC residue. The wafer was coated with the electron beam resist poly(methyl methacrylate) (PMMA) for patterning the contacts. After writing the contacts by electron-beam lithography, the patterned contacts were exposed to reactive ion etching to achieve 1D edge contacts<sup>46</sup>. Metallic contacts (5 nm Cr/60 nm Au) were made using thermal evaporation, followed by lift-off in warm acetone. Each device was etched into a Hall bar with six contacts - a schematic of the device structure with the probes (not to scale) is shown in Figure S5(a). The full structure was then encapsulated by another hBN (~25-40nm) and metallic (5 nm Cr/ 60 nm Au) top gates defined by electron-beam lithography. An optical image of one such complete device is shown in Figure S5(b).

The mobility of the device was found using equation  $\sigma = ne\mu$ , where  $\sigma$  is electrical conductivity  $n$  is charge number density,  $e$  is the electronic charge, and  $\mu$  is the mobility. The mobility fit is shown in Figure S5(d). The calculated mobility of the sample was  $\sim 1,12,000 \text{ cm}^2\text{V}^{-1}\text{s}^{-1}$  for holes and  $\sim 93,000 \text{ cm}^2\text{V}^{-1}\text{s}^{-1}$  for electrons.

### **Supplementary text 2: Hofstadter's butterfly and Moirè superlattice**

In the presence of both a periodic potential and a perpendicular magnetic field, the single-particle energy spectra show a recursive spectrum<sup>26,27,28</sup>. This spectrum is due to the interplay between the length scales associated with periodic potential (which in our case is the wavelength of the Moirè potential) and the magnetic length scale  $l_B = (\hbar/eB)^{1/2}$ . This recursive spectrum is known as Hofstadter's butterfly<sup>29,30,31,32</sup> and has been observed earlier in graphene superlattices<sup>26</sup>.

The 4-probe longitudinal magnetoconductivity ( $\sigma_{xx}$ ) was measured by varying the magnetic field and the back-gate voltage. The data are plotted in Figure S9. In the plot, the x-axis is the filling factor  $\nu$ , and the y-axis is  $\phi_0/\phi$ , which is the magnetic flux penetrating the unit cell of the superlattice<sup>26</sup>.  $\phi$  is given by  $B_{\perp} \times A$ ,  $B_{\perp}$  is the externally applied magnetic field perpendicular to the plane of the sample of area  $A$  and  $\phi_0 = h/e$ . The bright lines parallel to the x-axis at  $\phi_0/\phi = 2, 3, 4, 5, 6$  are independent of the filling factor and result from the formation of the fractal states in the presence of the magnetic field. The colour contrast lines parallel to the y-axis at  $\nu = \pm 4, \pm 8, \pm 12, \pm 16$  are quantum hall plateaus for the BLG<sup>49,50</sup>.

Figure S6(a) is a contour plot of logarithmic-scale longitudinal resistance conductivity  $\sigma_{xx}(B)$  as a function of the normalized carrier density ( $n/n_0$ ) and the normalized magnetic flux ( $\phi/\phi_0$ ) threading one Moirè super-lattice cell. Here,  $n_0$  is the number density required to fill the one

Moiré miniband,  $\phi = BA$  with  $B$  the applied perpendicular magnetic field and  $A$  the area of one Moiré unit cell,  $\phi_0 = h/e$  is the quantum flux quanta,  $h$  is Planck constant, and  $e$  the elementary charge. The measured dispersion of  $\sigma_{xx}(B)$  is characteristic of quantum Hall effect of BLG along with Landau-fan diagram of Hofstadter's butterfly; the latter arising due to the presence of a Moiré super-lattice potential<sup>29,30,31</sup>. The electron density  $n_s$  required to fill a Moiré mini-band is related to the angle  $\theta$  between the hBN and the BLG<sup>26</sup>. The angle  $\theta$  is related to the charge carrier density through the relation<sup>26</sup>  $n_s = \frac{8\theta^2}{\sqrt{3}a^2}$ , where  $a = 0.246$  nm is the graphene lattice constant. Using  $n_s = \frac{C_{BG}(V_{CDP}-V_{PDP})}{q}$ , the angle was found to be  $\theta = 0.91^\circ$ . Similarly, using the data of top gate scan, the angle was calculated to be  $\theta = 0.93^\circ$ .

### **Supplementary text 3: Effect of the SOI induced by WSe<sub>2</sub> in BLG**

#### **Determination of splitting in Fermi surface from SdH oscillations**

Figure S6(b) shows the plot of  $\sigma_{xx}(B)$  (with the background subtracted) as a function of the inverse of the applied magnetic field,  $1/B$  (measured for  $n = 2.3 \times 10^{16}$  m<sup>-2</sup> and  $|D| = 3.7 \times 10^8$  Vm<sup>-1</sup>). There is a clear beating pattern in the oscillations of  $\sigma_{xx}(B)$  (see also the splitting in the Fourier peaks plotted in Figure S6(c) indicating the splitting of the Fermi surface into two very closely-spaced ones. This is a consequence of the band-structure modification of BLG due to proximity-induced SOI<sup>51</sup>.

#### **Weak anti-localization in BLG**

Quantum interference of electronic wavefunctions leads to corrections to the Drude-Boltzmann conductivity. In bilayer graphene, which has a berry phase of  $2\pi$ , this leads to weak-localization in low-field magnetoconductance. On the other hand, when the BLG is placed in close physical contact with a TMDC, due to proximity induced spin-orbit coupling<sup>52,53,54,55,56,57</sup>, weak anti-localization (WAL) is observed. In Figure S8 Figure S8 is plotted the change in conductance of our device as a function of the magnetic field,  $\Delta\sigma = \sigma(B) - \sigma(0)$ . As expected, we observe WAL in our BLG/WSe<sub>2</sub> device, signifying strong proximity induced spin-orbit coupling in the BLG. The WAL data was fitted using the HLN equation<sup>58</sup>:

$$\Delta\sigma(B) = \sigma(B) - \sigma(0) = -\frac{e^2}{2\pi h} \left[ F\left(\frac{\tau_B^{-1}}{\tau_\phi^{-1}}\right) - F\left(\frac{\tau_B^{-1}}{\tau_\phi^{-1} + 2\tau_{asy}^{-1}}\right) - 2F\left(\frac{\tau_B^{-1}}{\tau_\phi^{-1} + \tau_{asy}^{-1} + \tau_{sym}^{-1}}\right) \right]$$

Here,  $F(x) = \ln(x) + \Psi\left(\frac{1}{2} + \frac{1}{x}\right)$ , with  $\Psi(x)$  the digamma function,  $\tau_B^{-1} = \frac{4eDB}{\hbar}$ ,  $D$  is the diffusion constant,  $\tau_\phi^{-1}$  is the coherent scattering rate,  $\tau_{asy}^{-1}$  is the scattering rate due to the spin-orbit coupling term that breaks the inversion symmetry about the  $z$ -axis.  $\tau_{sym}^{-1}$  is the scattering rate due to SOI that preserves the inversion symmetry about the  $z$ -axis. The fit is shown in Figure S8 by the red line. From the fit, the spin scattering time  $\tau_{sym}$  was found to be 23 ps.

## **Supplementary text 4: Extended data and Landauer Büttiker formalism**

### **Reproducibility of the 2-probe and 4-probe quantization data**

The quantization of the 4-probe 2-probe longitudinal resistance were measured to be reproducible over different cool downs. Figure S7(c) shows the four-probe longitudinal resistance as a function of top gate voltage for different back-gate voltages at  $\sim 20$  mK for the first cool down. The maxima in  $R$  is at number density  $n \sim 0$  and displacement field  $0.47 \times 10^9 \text{ V m}^{-1} < |D| < 0.54 \times 10^9 \text{ V m}^{-1}$ . It was found to be quantized to  $h/(2e^2)$ . At these values of  $n$  and  $D$ , the chemical potential lies in the bulk bandgap, and we are probing purely edge state. Figure S7(d) is the data at the same temperature from another cool down – in this case also the quantization of the 4-probe longitudinal resistance to  $h/(2e^2)$  is seen.

### **Measurements in multi-terminal configurations**

We measured the resistance of the device as a function of gate voltage in different configurations, the data are plotted in Figure S7(b). We used Landauer Büttiker (LB) formalism<sup>59</sup> of quantum transport to calculate the resistance in these measurement configurations considering helical edge. The calculations were done by considering a 6-terminal hall device that mimics our device geometry – a schematic of the device structure with the probes (not to scale) is shown in Figure S7(a). For a multiprobe conductor, the net current flowing into the  $i^{\text{th}}$  contact to all other contacts is given by:

$$I_i = \sum_j (T_{j \leftarrow i} \mu_i - T_{i \leftarrow j} \mu_j) = \frac{e^2}{h} \sum_j (M_{j \leftarrow i} V_i - M_{i \leftarrow j} V_j) \quad \text{---(1)}$$

where  $\mu_i$  is the potential of the  $i^{\text{th}}$  contact and  $M_{j \leftarrow i}$  is the number of modes going from contact  $i$  to  $j$ . Equation (1) can be written in a matrix form as:

$$\begin{pmatrix} I_1 \\ I_2 \\ I_3 \\ I_4 \\ I_5 \\ I_6 \end{pmatrix} = \frac{e^2}{h} \begin{pmatrix} 2 & -1 & 0 & 0 & 0 & -1 \\ -1 & 2 & -1 & 0 & 0 & 0 \\ 0 & -1 & 2 & -1 & 0 & 0 \\ 0 & 0 & -1 & 2 & -1 & 0 \\ 0 & 0 & 0 & -1 & 2 & -1 \\ -1 & 0 & 0 & 0 & -1 & 2 \end{pmatrix} \begin{pmatrix} V_1 \\ V_2 \\ V_3 \\ V_4 \\ V_5 \\ V_6 \end{pmatrix} \quad \text{---(2)}$$

Below we use solve Equation (2) for each configuration and compare the results with the experimental observations

#### Four-probe longitudinal resistance:

For the measurement of 4-probe longitudinal resistance, the current is injected from contact 1, contact number 4 is grounded, and all other contacts are the voltage probes. The voltage matrix in this case is:

$$\begin{pmatrix} V_1 \\ V_2 \\ V_3 \\ V_5 \\ V_6 \end{pmatrix} = \frac{h}{e^2} I \begin{pmatrix} 2 & -1 & 0 & 0 & -1 \\ -1 & 2 & -1 & 0 & 0 \\ 0 & -1 & 2 & 0 & 0 \\ 0 & 0 & 0 & 2 & -1 \\ -1 & 0 & 0 & -1 & 2 \end{pmatrix}^{-1} \begin{pmatrix} 1 \\ 0 \\ 0 \\ 0 \\ 0 \end{pmatrix}$$

$$\begin{pmatrix} V_1 \\ V_2 \\ V_3 \\ V_5 \\ V_6 \end{pmatrix} = \frac{h}{e^2} I \begin{pmatrix} 1.5 \\ 1.0 \\ 0.5 \\ 0.5 \\ 1.0 \end{pmatrix}$$

The 4-probe resistance is:  $R_{23,14} = R_{65,14} = \frac{V_2 - V_3}{I} = \frac{1}{2} \frac{h}{e^2}$ . As shown in Figure S7(b) by solid green line (also in Figure 4 of the main text), these values match exceptionally well with our experimental results measured result over a range of electric field near the primary Dirac point,  $n \approx 0$ .

#### Two-probe longitudinal resistance:

For current injected from contact number 3 and contact number 4 grounded, equation 2 becomes:

$$\begin{pmatrix} V_1 \\ V_2 \\ V_3 \\ V_5 \\ V_6 \end{pmatrix} = \frac{h}{e^2} I \begin{pmatrix} 2 & -1 & 0 & 0 & -1 \\ -1 & 2 & -1 & 0 & 0 \\ 0 & -1 & 2 & 0 & 0 \\ 0 & 0 & 0 & 2 & -1 \\ -1 & 0 & 0 & -1 & 2 \end{pmatrix}^{-1} \begin{pmatrix} 0 \\ 0 \\ 1 \\ 0 \\ 0 \end{pmatrix}$$

$$\begin{pmatrix} V_1 \\ V_3 \\ V_4 \\ V_5 \\ V_6 \end{pmatrix} = \frac{h}{e^2} I \begin{pmatrix} 0.500 \\ 0.667 \\ 0.833 \\ 0.166 \\ 0.333 \end{pmatrix}$$

$$R_{34,34} = \frac{V_3 - V_4}{I} = \frac{5 h}{6 e^2}$$

This matches very well with the measured result at  $n = 0$  shown in Figure S7 (b) by the solid red line.

Similarly, for the set of two probes 1 and 4, equation 2 can be written as:

$$\begin{pmatrix} V_1 \\ V_2 \\ V_3 \\ V_5 \\ V_6 \end{pmatrix} = \frac{h}{e^2} I \begin{pmatrix} 2 & -1 & 0 & 0 & -1 \\ -1 & 2 & -1 & 0 & 0 \\ 0 & -1 & 2 & 0 & 0 \\ 0 & 0 & 0 & 2 & -1 \\ -1 & 0 & 0 & -1 & 2 \end{pmatrix}^{-1} \begin{pmatrix} 1 \\ 0 \\ 0 \\ 0 \\ 0 \end{pmatrix}$$

$$\begin{pmatrix} V_1 \\ V_2 \\ V_3 \\ V_5 \\ V_6 \end{pmatrix} = \frac{h}{e^2} I \begin{pmatrix} 1.5 \\ 1.0 \\ 0.5 \\ 0.5 \\ 1.0 \end{pmatrix}$$

This gives  $R_{14,14} = \frac{V_1 - V_4}{I} = \frac{3 h}{2 e^2}$ . The results are plotted in Figure S7(b) by the solid black line.

Resistance in multi-probe configurations:

The blue line shown in Figure S7(b) is the result of measurements in the following configuration: voltage measured between contacts 1 and 3 by injecting current in contact 6 and grounding contact 4. From equation 2, we can again write the matrix equation as follows:

$$\begin{pmatrix} V_1 \\ V_2 \\ V_3 \\ V_5 \\ V_6 \end{pmatrix} = \frac{h}{e^2} I \begin{pmatrix} 2 & -1 & 0 & 0 & -1 \\ -1 & 2 & -1 & 0 & 0 \\ 0 & -1 & 2 & 0 & 0 \\ 0 & 0 & 0 & 2 & -1 \\ -1 & 0 & 0 & -1 & 2 \end{pmatrix}^{-1} \begin{pmatrix} 0 \\ 0 \\ 0 \\ 0 \\ 1 \end{pmatrix}$$

$$\begin{pmatrix} V_1 \\ V_2 \\ V_3 \\ V_5 \\ V_6 \end{pmatrix} = \frac{h}{e^2} I \begin{pmatrix} 1.0000 \\ 0.6667 \\ 0.3333 \\ 0.6667 \\ 1.3333 \end{pmatrix}$$

From the above matrix, the resistance can be extracted to be:

$$R_{13,64} = \frac{V_1 - V_3}{I} = \frac{2 h}{3 e^2}$$

The measured data are plotted in solid blue line in Figure S7(b).

Thus, in several different configurations, the measured resistance matches exceptionally well with the value expected for helical edge-modes with one set of counter-propagating 1-D channels at each edge.

### **Supplementary text 5: Calculations of edge and bulk dispersion relations**

We construct a tight-binding model with spin-orbit coupling (SOI) for the AB-stacked (Bernal stacking) BLG on WSe<sub>2</sub> heterostructure. The model Hamiltonian is:

$$H = H_{\text{TB}} + H_{\text{SOC}} \quad (1)$$

Here  $H_{\text{TB}}$  gives the tight-binding model for bilayer graphene, and  $H_{\text{SOC}}$  is the SOI term.  $H_{\text{TB}}$  is given by:

$$H_{\text{TB}} = \sum_{\langle ij \rangle, \sigma} t c_{i\sigma,1}^\dagger c_{j\sigma,1} + t c_{i\sigma,2}^\dagger c_{j\sigma,2} + t' c_{i\sigma,1}^\dagger c_{j\sigma,2} + \text{h.c} \quad (2)$$

where  $c_{i\sigma,\gamma}^\dagger$  and  $c_{i\sigma,\gamma}$  are creation and annihilation operators at lattice site  $i$  with  $\sigma$  and  $\gamma$  indices representing spin and layer, respectively.  $t(t')$  is the nearest neighbor intra(inter)-layer hopping parameter,  $c_{i\sigma,\gamma}^\dagger$  is a spinor, decomposed in the sublattice basis  $c_{i\sigma,\gamma}^\dagger = a_{i\sigma,\gamma}^\dagger b_{i\sigma,\gamma}^\dagger$ . So we obtain

$$H_{\text{TB}} = \sum_{\langle ij \rangle, \sigma} t (a_{i\sigma,1}^\dagger b_{j\sigma,1} + a_{i\sigma,2}^\dagger b_{j\sigma,2}) + t' a_{i\sigma,1}^\dagger b_{j\sigma,2} + \text{h.c} \quad (3)$$

where  $a_{i\sigma,\gamma}^\dagger$  and  $a_{j\sigma,\gamma}$  ( $b_{i\sigma,\gamma}^\dagger$  and  $b_{j\sigma,\gamma}$ ) are creation and annihilation operators at sublattice site  $a(b)$ .

We include a mirror-symmetric SOI via a spin-dependent second nearest neighbor hopping term

$$H_{\text{SOC}} = i\lambda_{\text{SO},\gamma} \sum_{\langle\langle ij \rangle\rangle, \sigma, \gamma} v_{ij} c_{i\sigma,\gamma}^\dagger s_z c_{j\sigma,\gamma} \quad (4)$$

Where  $\lambda_{\text{SO}}$  is spin-orbit coupling strength,  $s_z$  is given by Pauli spin matrix indicating the spin ( $\pm\sigma_z$ ).  $v_{ij} = \frac{2}{\sqrt{3}}(\mathbf{d}_i \times \mathbf{d}_j)$ , where  $\mathbf{d}_i$  and  $\mathbf{d}_j$  are the unit vectors in the direction of two bonds that the electron traverses in going from the site  $i$  to site  $j$ .

In our case of BLG /WSe<sub>2</sub> heterostructure, earlier studies have suggested the appearance of a strong SOI in the graphene layer next to WSe<sub>2</sub> and a weaker SOI in other graphene layers<sup>14</sup>. We study the effect of an applied transverse electric field on the heterostructure by including positive and negative chemical potential shifts in the two graphene layers. If  $V$  is the voltage

difference due to the applied electric field between two layers, then our tight-binding Hamiltonian becomes:

$$H_{TB} = \sum_{\langle ij \rangle, \sigma} t(a_{i\sigma,1}^\dagger b_{j\sigma,1} + a_{i\sigma,2}^\dagger b_{j\sigma,2}) + t' a_{i\sigma,1}^\dagger b_{j\sigma,2} + \text{h.c} + \sum_{i,\sigma} \frac{V}{2} (a_{i\sigma,1}^\dagger a_{i\sigma,1} + b_{i\sigma,1}^\dagger b_{i\sigma,1} - a_{i\sigma,2}^\dagger a_{i\sigma,2} - b_{i\sigma,2}^\dagger b_{i\sigma,2}) \quad (5)$$

To get the band structure for our model from eq. 1 together with eq. 5, we first do a Fourier transformation. In k-space our Hamiltonian takes the form:

$$H = C_{\mathbf{k}}^\dagger H(\mathbf{k}) C_{\mathbf{k}}, \quad (6)$$

with

$$C_{\mathbf{k}}^\dagger = (a_{\mathbf{k}\uparrow 1}^\dagger b_{\mathbf{k}\uparrow 1}^\dagger a_{\mathbf{k}\downarrow 1}^\dagger b_{\mathbf{k}\downarrow 1}^\dagger a_{\mathbf{k}\uparrow 2}^\dagger b_{\mathbf{k}\uparrow 2}^\dagger a_{\mathbf{k}\downarrow 2}^\dagger b_{\mathbf{k}\downarrow 2}^\dagger) \quad (7)$$

We write

$$H(\mathbf{k}) = \begin{bmatrix} H_1 & D \\ D' & H_2 \end{bmatrix}, \quad (8)$$

$$H_1 = \begin{bmatrix} \epsilon_{\text{SOC}}^1 - \frac{V}{2} & 0 & \epsilon_{\mathbf{k}} & 0 \\ 0 & -\epsilon_{\text{SOC}}^1 - \frac{V}{2} & 0 & \epsilon_{\mathbf{k}} \\ \epsilon_{\mathbf{k}} & 0 & -\epsilon_{\text{SOC}}^1 - \frac{V}{2} & 0 \\ 0 & \epsilon_{\mathbf{k}} & 0 & \epsilon_{\text{SOC}}^1 - \frac{V}{2} \end{bmatrix} \quad (9)$$

$$H_2 = \begin{bmatrix} \epsilon_{\text{SOC}}^2 + \frac{V}{2} & 0 & \epsilon_{\mathbf{k}} & 0 \\ 0 & -\epsilon_{\text{SOC}}^2 + \frac{V}{2} & 0 & \epsilon_{\mathbf{k}} \\ \epsilon_{\mathbf{k}} & 0 & -\epsilon_{\text{SOC}}^2 + \frac{V}{2} & 0 \\ 0 & \epsilon_{\mathbf{k}} & 0 & \epsilon_{\text{SOC}}^2 + \frac{V}{2} \end{bmatrix} \quad (10)$$

$$D = \begin{bmatrix} 0 & 0 & 0 & 0 \\ 0 & 0 & 0 & 0 \\ 0 & -t' & 0 & 0 \\ -t' & 0 & 0 & 0 \end{bmatrix} \quad (11)$$

Where  $D'$  is the transpose of  $D$ , and

$$\epsilon_{\mathbf{k}} = -t \left( 2 \exp\left(\frac{-ik_y}{2\sqrt{3}}\right) \cos \frac{k_x}{2} + \exp\left(\frac{ik_y}{\sqrt{3}}\right) \right), \quad (12)$$

$$\epsilon_{\text{SOC}}^i = \lambda_{\text{SO},i} \left( 2 \sin k_x - 4 \sin \frac{k_x}{2} \cos \frac{\sqrt{3}k_y}{2} \right), \quad (13)$$

Diagonalizing the matrix  $H(\mathbf{k})$ , we get the band structure for our model (see Figure S10). In all our calculation we used  $t = 2.78\text{eV}$ ,  $t' = 0.37\text{eV}$ ,  $\lambda_{\text{SOC},1} = 2\text{meV}$  and  $\lambda_{\text{SOC},2} = 20\mu\text{eV}$ .

For bulk band structure, we focus our study on the four bands nearest to the Fermi level around the K point (Figure S10(c-e) first two rows). For no applied electric field (first row) we find from Figure S10(d) that the top and bottom bands have band weight contributions from the high-SOI layer, and consequently, they are spin-split. The middle two bands are nearly degenerate around the K point because of their band weight contribution is from the low-SOI layer. As we apply an electric field, the band weight gets redistributed, and for positive field Figure S10(e), the upper two layers are spin-split as their band weight contribution comes from high SOI layer while the lower two bands are almost degenerate. For negative electric fields, (Figure S10(c)) opposite effect is observed. Similar observations were reported in an earlier DFT study<sup>14</sup>. We show our edge state calculation in the third row of Figure S10(c–e). We can see the presence of edge states in the bulk bandgap region. For no applied electric field, the edge-states are nearly flat, indicating that they carry negligible current. For finite  $|D|$ , these states become dispersive and can carry current. We show the spin splitting of the edge states in the fourth row of Figure S10, which shows the presence of two counter-propagating states with an opposite spin at each edge.

## **Supplementary text 6: Presence of non-local signal and edge transport**

### Ohmic contribution to non-local signal:

For electronic systems which have the finite Berry curvature, besides the conventional band velocity  $v_B \left( = \frac{1}{\hbar} \frac{\partial E}{\partial k} \right)$ , the charge carriers gain an anomalous velocity given<sup>60</sup> by  $d\mathbf{p}/dt \times \Omega_{\text{Berry}}$ . This anomalous velocity does not depend on the charge degree of freedom; instead, it is related to a spin or pseudospin degree of freedom - like the site-, layer- or valley-degree of freedom. This anomalous velocity will lead to a non-local signal<sup>55,61,62</sup> in these systems. However, in addition to the topological origin, there can also be some ohmic contribution to the non-local signal<sup>61,62,63</sup>. The value of this ohmic component is generally minimal compared to the non-local signal of topological one. The measured non-local signal and calculated ohmic contribution are plotted in Figure S11(a) – one can see that the ohmic contribution to the signal is indeed very small as compared to the total measured  $R_{\text{NL}}$ . This eliminates ohmic diffusive current as the origin of the observed non-local signal in our measurements.

### B-field dependence of $R_{NL}$ :

The non-local resistance  $R_{NL}$  signal was measured as a function of the magnetic field,  $B$  applied perpendicular to the plane of the device. As  $B$ -field breaks TR symmetry, it should lead to a quenching of the QSH state and consequent decay of the non-local signal. However, the non-local signal can persist as long as<sup>39,64</sup>  $2\Delta > 2E_Z$ , where  $\Delta$  is the energy-gap for the QSH state and  $E_Z$  is the Zeeman energy given by  $E_Z(B) = 0.5g^*\mu_B B$ . Here  $g^*$  is the effective  $g$ -factor and  $\mu_B$  is the Boltzmann constant. The effective  $g$ -can be estimated from  $g^* = (2mv_F^2)/\Delta$ , where  $m$  is the mass of the free electron and  $v_F$  is the Fermi-velocity in the band. Thus, the maximum perpendicular magnetic field till which one would expect the QSH state to persist is given by:

$$B_{\max} = \frac{\Delta^2}{m\mu_B v_F^2}$$

From measurements of the temperature dependence of the 4-probe conductance,  $\Delta$  was estimated to be approximately 7 meV. Using  $v_F = 1.2 \times 10^6 \text{ ms}^{-1}$ , one gets  $B_{\max} \sim 0.1 \text{ T}$ . A plot of the  $B$ -field dependence of the quantized 4-probe longitudinal resistance is shown in Figure S11(b). One can see that the quantization breaks down beyond about 0.1-0.2 T establishing the correctness of the estimate of  $\Delta$ . Measurements of  $R_{NL}$  in the presence of a perpendicular magnetic field show that the non-local signal appears only near the PDP for  $B \sim 0$  (Figure S11(c)). On the other hand,  $R_{NL}$  is completely absent at the CDP over the field range  $-0.1 \text{ T} < B < 0.1 \text{ T}$  – beyond this field range Quantum Hall sets in.

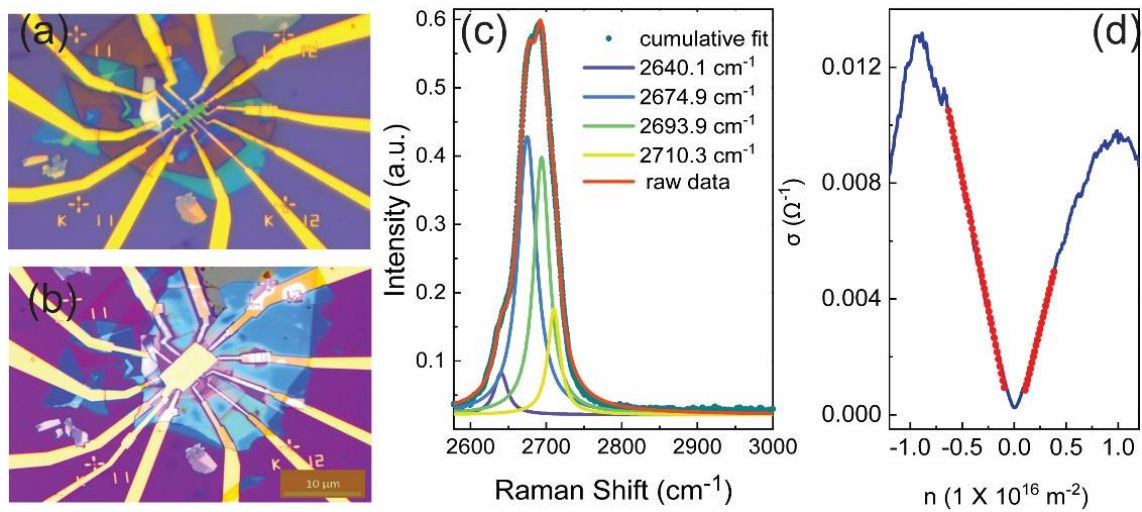


Figure S5: (a) Optical image of the device (in 100X magnification) after hall bar etching and metallization of the contact pads. (b) Optical image of the device (in 100X magnification) after adding the top gate. (c) Spectral decomposition of the 2D peak of BLG showing the four Lorentzian components. (d) The solid blue line indicates the measured 4-probe conductance plotted versus the charge carrier number density. The dotted red lines are linear fits to the equation  $\sigma = ne\mu$ . The data were taken at T=20 mK and B= 0 T.

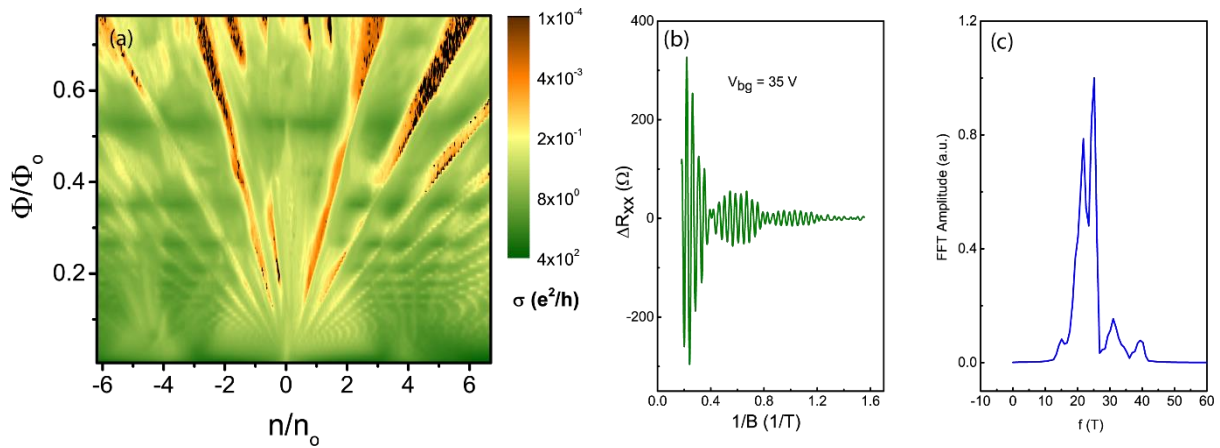


Figure S6: Lifting of the degeneracies. (a) A logarithmic scale plot of the 4-probe longitudinal conductivity  $\sigma_{xx}$  as a function of charge-carrier density  $n$  (normalized by  $n_0$  - the number density required to fill the one Moiré miniband) and the flux  $\phi$  (normalized by  $\phi_0 = h/e$  - the quantum flux quanta) threading the device. In addition to the usual Landau fan diagram emanating from  $n/n_0 = 0$ , one can see two additional sets of fans originating at  $n/n_0 = \pm 0$ . These are the Landau levels corresponding to the Moiré sub-bands. (b) Shubnikov-de Haas (SdH) oscillations plotted versus  $1/B$  - a beating pattern can clearly be seen. (c) Fourier transform of the SdH oscillations showing the appearance of two closely spaced peaks. All the data were acquired at  $T = 20 \text{ mK}$ .

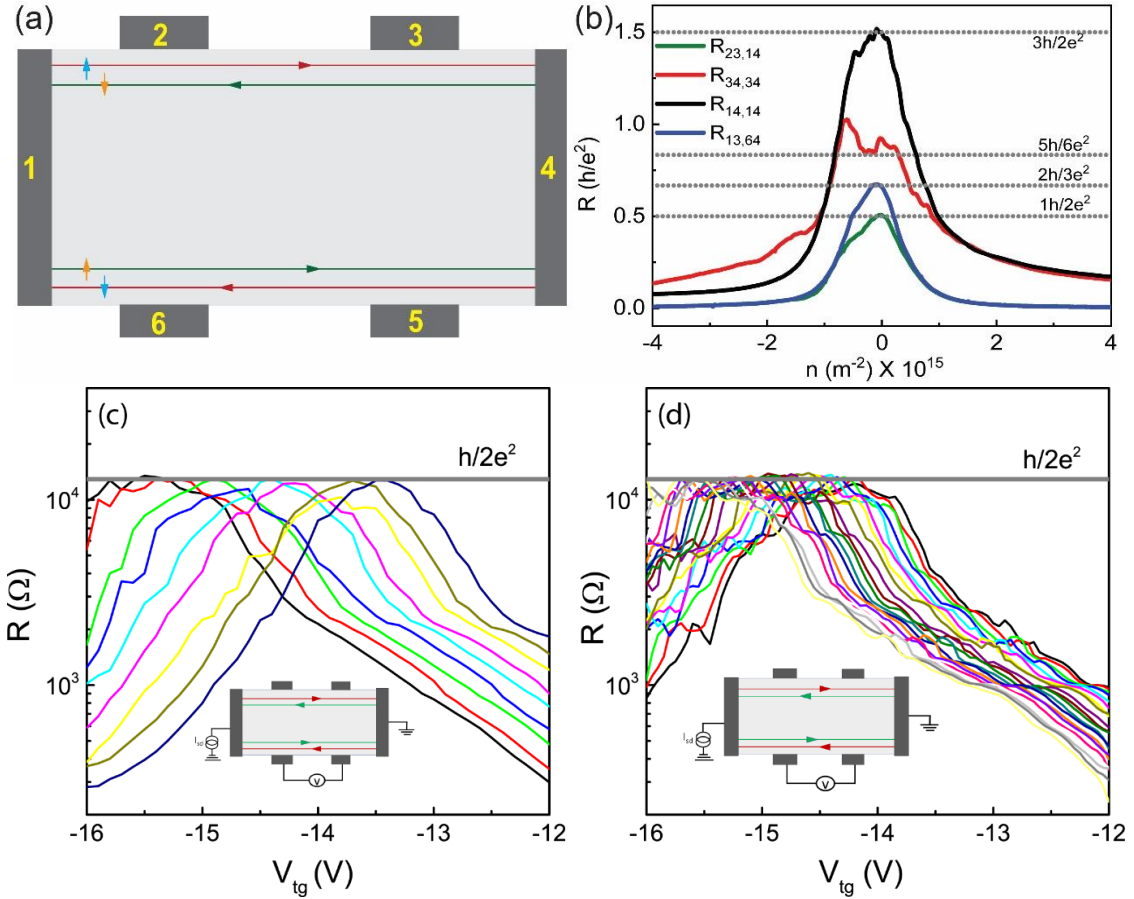


Figure S7: (a) Schematic of 6-terminal device showing the numbering of the contacts. (b) Resistance measured in different configurations plotted versus charge carrier number density. Black line:  $R_{14,14}$ , green line:  $R_{23,14}$ , red line:  $R_{34,34}$  and blue line:  $R_{13,64}$ . In each case, the notation  $R_{ij,kl}$  represents a configuration where the current is injected at the  $k^{\text{th}}$  contact,  $l^{\text{th}}$  contact is grounded, and the voltage drop is measured between the  $i^{\text{th}}$  and the  $j^{\text{th}}$  contacts. The grey dotted line in each case is the value expected for helical QSH modes. (c) Quantization of the 4-probe resistance to  $h/(2e^2)$  at several values of  $V_{tg}$  for fixed value of  $V_{bg}$  for the first cool down. (d) Quantization of 4 probe resistance to  $h/(2e^2)$  at several values of  $V_{tg}$  for fixed value of  $V_{bg}$  for the second cool down. The data in (c) and (d) were all taken at  $T = 20$  mK and at  $B = 0$ .

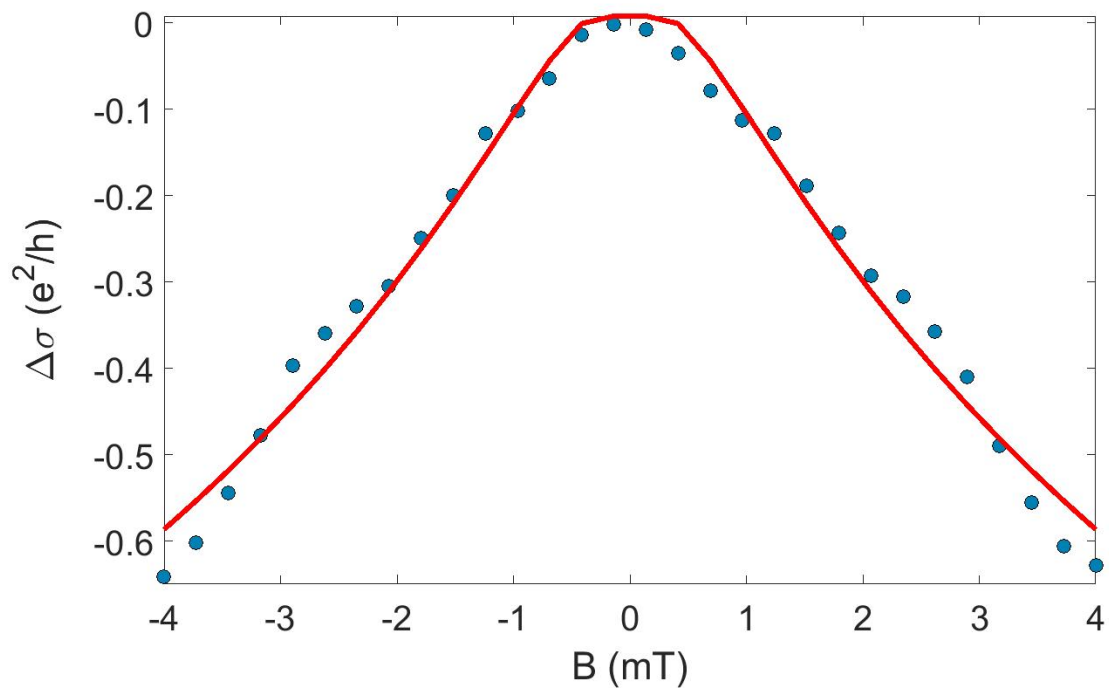


Figure S8: Weak antilocalization fit to the negative magnetoconductance – the measurements were done at  $T = 20$  mK. The measured data are shown in blue filled circles; the solid red line is the HLN fit to the data.

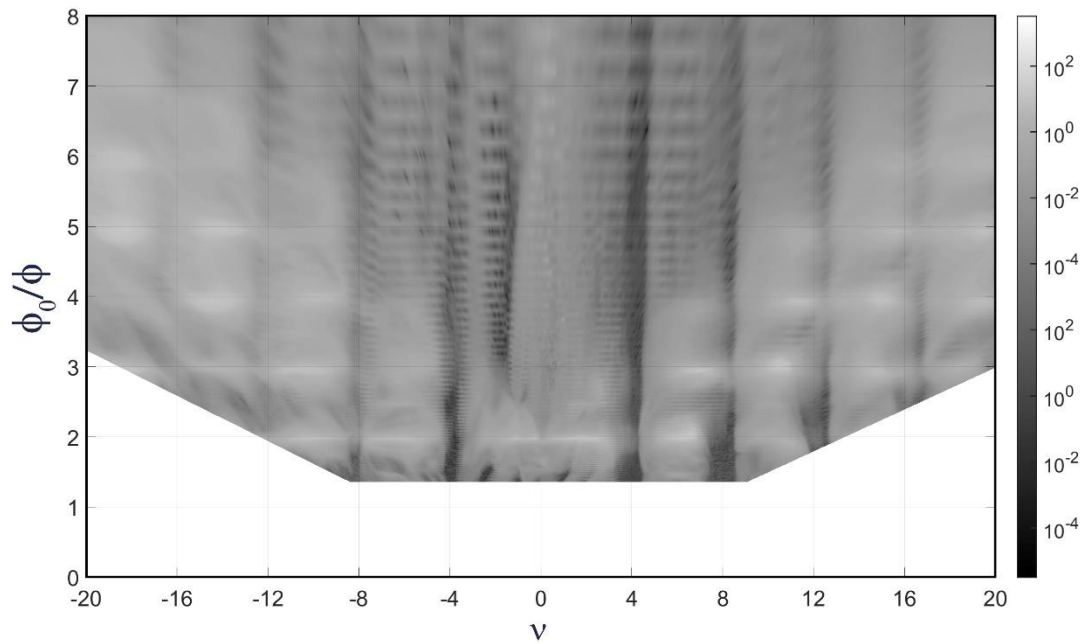


Figure S9: Fractal pattern observed in longitudinal conductivity in a perpendicular magnetic field. In the plot, the x-axis is the filling factor  $\nu$ , and the y-axis is  $\phi_0/\phi$  which is the magnetic flux penetrating the unit cell of the superlattice.  $\phi$  is given by  $B_{\perp} \times A$ ,  $B_{\perp}$  is the externally applied magnetic field perpendicular to the plane of the sample of area  $A$  and  $\phi_0 = h/e$ . The bright lines parallel to the x-axis at  $\phi_0/\phi = 2, 3, 4, 5, 6\dots$  are independent of the filling factor and result from the formation of the fractal states in the presence of the magnetic field. The colour contrast lines parallel to the y-axis at  $\nu = \pm 4, \pm 8, \pm 12, \pm 16$  are quantum hall plateaus for the BLG.

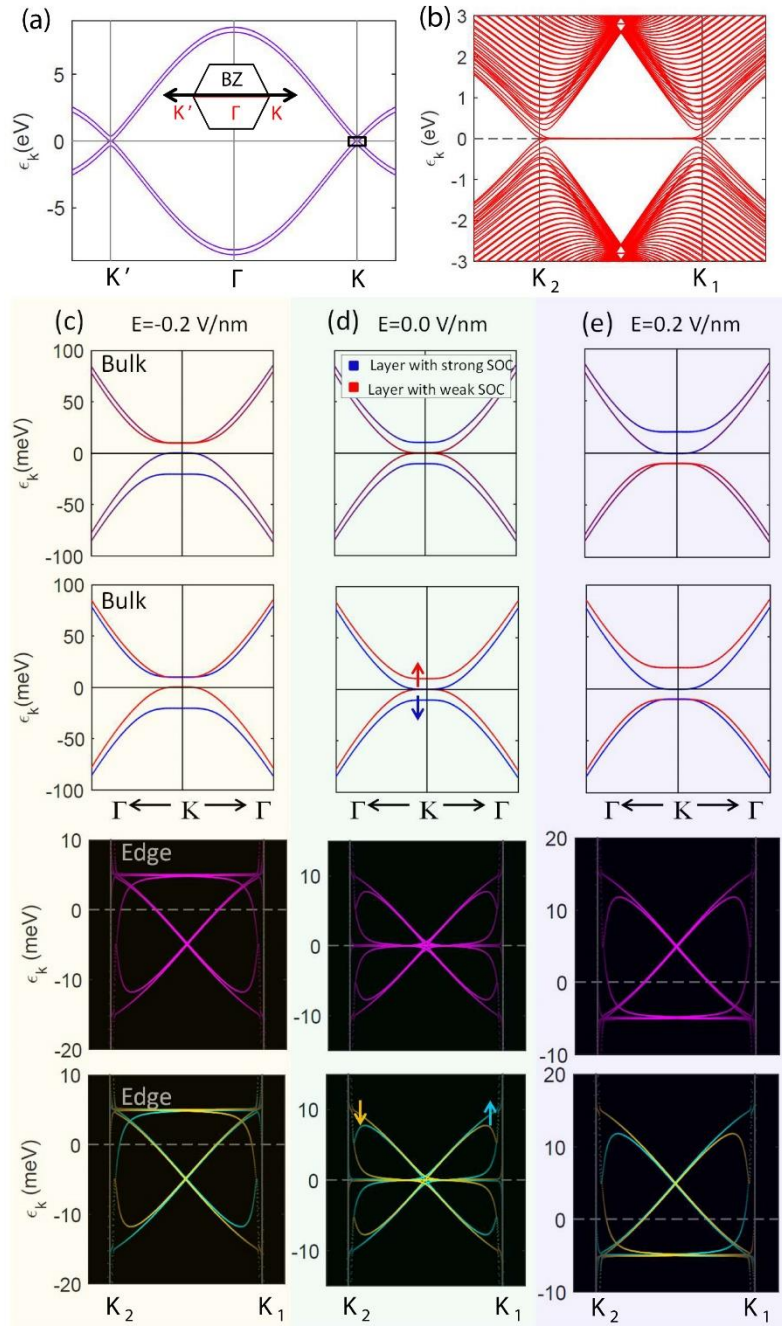


Figure S10: (a) Bulk band structure and (b) edge modes for BLG/WSe<sub>2</sub> heterostructure. Bulk band structure and edge modes plotted near the  $K$ -point for applied displacement field (c)  $-0.2$  V/nm, (d)  $0$  V/nm, and (e)  $0.2$  V/nm. The first row shows the bulk band structure with band weight contribution from different layers zoomed around  $K$  point as indicated by a small square box in (a). The second row shows the spin-splitting of the bulk bands around the  $K$  point. The third row shows zoomed edge states, as indicated by a small square box in (b). The fourth row shows the spin splitting of the edge states.

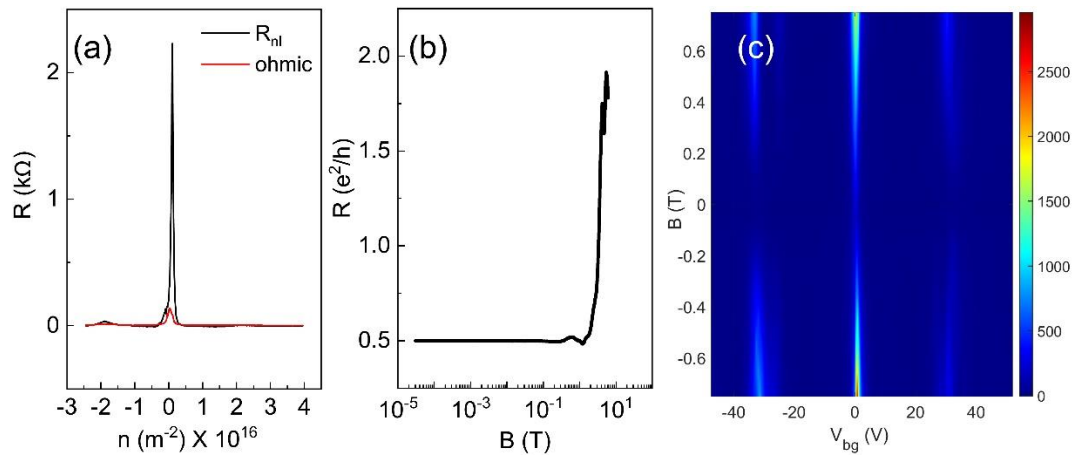


Figure S11: (a) Plot of non-local resistance versus top-gate voltage  $V_{tg}$ . The solid red line is a plot of the estimated maximum ohmic contribution to  $R_{NL}$  from diffusive transport. (b) Magnetic field dependence of the 4-probe quantized resistance for  $B$  perpendicular to the device plane. (c) A plot of  $R_{NL}$  versus  $B$  and  $V_{bg}$ .

## References

- <sup>1</sup> B. I. Halperin, Quantized Hall conductance, current-carrying edge states, and the existence of extended states in a two-dimensional disordered potential. *Phys. Rev. B* 25, 2185(1982).
- <sup>2</sup> Yasuhiro Hatsugai, Edge states in the integer quantum Hall effect and the Riemann surface of the Bloch function. *Phys. Rev. B* 48, 11851(1993).
- <sup>3</sup> Yasuhiro Hatsugai, Chern Number and Edge States in the Integer Quantum Hall Effect. *Phys. Rev. Lett.* 71, 3697(1993).
- <sup>4</sup> Thouless, D. J., Kohmoto, M., Nightingale, M. P. & den Nijs, M. Quantized hall conductance in a two-dimensional periodic potential. *Physical Review Letters* 49, 405 (1982).
- <sup>5</sup> Wen, X.-G. Topological orders and edge excitations in fractional quantum hall states. *Advances in Physics* 44, 405–473 (1995).
- <sup>6</sup> Dmitry A. Abanin, Patrick A. Lee, and Leonid S. Levitov, Spin-Filtered Edge States and Quantum Hall Effect in Graphene. *Phys. Rev. Lett.* PRL 96, 106 (2006).
- <sup>7</sup> C. L. Kane and E. J. Mele, Z<sub>2</sub> Topological Order and the Quantum Spin Hall Effect. *Phys. Rev. Lett.* 95, 146802 (2005).
- <sup>8</sup> C. L. Kane and E. J. Mele, Quantum Spin Hall Effect in Graphene. *Phys. Rev. Lett.* 95, 226801 (2005).
- <sup>9</sup> B. Andrei Bernevig and Shou-Cheng Zhang, Quantum Spin Hall Effect. *Phys. Rev. Lett.* 96, 106802 (2006).
- <sup>10</sup> Conan Weeks, Jun Hu, Jason Alicea, Marcel Franz, and Ruqian Wu, Engineering a Robust Quantum Spin Hall State in Graphene via Adatom Deposition. *Phys. Rev. X* 1, 021001 (2011).
- <sup>11</sup> K. Hatsuda, H. Mine, T. Nakamura, J. Li, R. Wu, S. Katsumoto and J. Haruyama, Evidence for a quantum spin Hall phase in graphene decorated with Bi<sub>2</sub>Te<sub>3</sub> nanoparticles. *Science Advances*, 4, eaau6915(2018).
- <sup>12</sup> T. Wakamura, F. Reale, P. Palczynski, S. Guéron, C. Mattevi, and H. Bouchiat, Strong Anisotropic Spin-Orbit Interaction Induced in Graphene by Monolayer WS<sub>2</sub>. *Phys. Rev. Lett.* 120, 106802(2018).
- <sup>13</sup> Zhe Wang, Dong-Keun Ki, Jun Yong Khoo, Diego Mauro, Helmuth Berger, Leonid S. Levitov, and Alberto F. Morpurgo, Origin and Magnitude of ‘Designer’ Spin-Orbit Interaction in Graphene on Semiconducting Transition Metal Dichalcogenides. *Phys. Rev. X* 6, 041020(2016).
- <sup>14</sup> Martin Gmitra and Jaroslav Fabian, Proximity Effects in Bilayer Graphene on Monolayer WSe<sub>2</sub>: Field-Effect Spin Valley Locking, Spin-Orbit Valve, and Spin Transistor. *Phys. Rev. Lett.* 119, 146401(2017).
- <sup>15</sup> Markus König, Steffen Wiedmann, Christoph Brüne, Andreas Roth, Hartmut Buhmann, Laurens W. Molenkamp, Xiao-Liang Qi, Shou-Cheng Zhang, Quantum Spin Hall Insulator State in HgTe Quantum Wells. *Science* 318, 766-770(2007).
- <sup>16</sup> Andreas Roth, Christoph Brüne, Hartmut Buhmann, Laurens W. Molenkamp, Joseph Maciejko, Xiao-Liang Qi, Shou-Cheng Zhang, *Science* 325, 294-297(2009).
- <sup>17</sup> Ivan Knez, Rui-Rui Du, and Gerard Sullivan, Evidence for Helical Edge Modes in Inverted InAs/GaSb Quantum Wells. *Phys. Rev. Lett.* 107, 136603(2011).
- <sup>18</sup> Kyoichi Suzuki, Yuichi Harada, Koji Onomitsu, and Koji Muraki, Edge channel transport in the InAs/GaSb topological insulating phase. *Phys. Rev. B* 87, 235311(2013).
- <sup>19</sup> Fabrizio Nichele, Atindra Nath Pal, Patrick Pietsch, Thomas Ihn, Klaus Ensslin, Christophe Charpentier, and Werner Wegscheider, Insulating State and Giant Nonlocal Response in an InAs/GaSb Quantum Well in the Quantum Hall Regime. *Phys. Rev. Lett.* 112, 036802(2014).
- <sup>20</sup> Lingjie Du, Ivan Knez, Gerard Sullivan, and Rui-Rui Du, Robust Helical Edge Transport in Gated InAs/GaSb Bilayers. *Phys. Rev. Lett.* 114, 096802(2015)

- 
- <sup>21</sup> Filippo Pizzocchero, Lene Gammelgaard, Bjarke S. Jessen, José M. Caridad, Lei Wang, James Hone, Peter Bøggild, Timothy J. Booth, The hot pick-up technique for batch assembly of van der Waals heterostructures. *Nature Communications* 7, Article number: 11894 (2016).
- <sup>22</sup> Weijie Zhao, Zohreh Ghorannevis, Kiran Kumar Amara, Jing Ren Pang, Minglin Toh, Xin Zhang, Christian Kloc, Ping Heng Tan and Goki Eda, lattice dynamics in mono and few layer sheets of WS<sub>2</sub> and WSe<sub>2</sub>, *Nano Scale*, 5, 9677-9682(2013).
- <sup>23</sup> L.M.Malard, M.A.Pimenta, G.Dresselhaus, M.S.Dresselhaus, Raman spectroscopy in graphene, *Physics Report*, 473, 51-87(2009).
- <sup>24</sup> Philipp Tonndorf, Robert Schmidt, Philipp Böttger, Xiao Zhang, Janna Börner, Andreas Liebig, Manfred Albrecht, Christian Kloc, Ovidiu Gordan, Dietrich R. T. Zahn, Steffen Michaelis de Vasconcellos, and Rudolf Bratschitsch, Photoluminescence emission in Raman response of mono layer MOS<sub>2</sub>, MOSe<sub>2</sub> and WSe<sub>2</sub>, *Optics Express*, 21, 49082-4916(2013).
- <sup>25</sup> L. A. Ponomarenko, R. V. Gorbachev, G. L. Yu, D. C. Elias, R. Jalil, A. A. Patel, A. Mishchenko, A. S. Mayorov, C. R. Woods, J. R. Wallbank, M. Mucha-Kruczynski, B. A. Piot, M. Potemski, I. V. Grigorieva, K. S. Novoselov, F. Guinea, V. I. Fal'ko and A. K. Geim, Cloning of Dirac fermions in graphene superlattices. *Nature* 497, 594–597(2013).
- <sup>26</sup> C. R. Dean, L. Wang, P. Maher, C. Forsythe, F. Ghahari, Y. Gao, J. Katoch, M. Ishigami, P. Moon, M. Koshino, T. Taniguchi, K. Watanabe, K. L. Shepard, J. Hone, and P. Kim, Hofstadter's butterfly and the fractal quantum Hall effect in moiré superlattices. *Nature* 497, 598–602(2013).
- <sup>27</sup> Hofstadter, D. Energy levels and wave functions of Bloch electrons in rational and irrational magnetic fields. *Phys. Rev.* B14,2239–2249 (1976).
- <sup>28</sup> Thouless, D. J, Kohmoto, M., Nightingale, M. & denNijs, M. Quantized Hall conductance in a two-dimensional periodic potential. *Phys. Rev. Lett.* 49,405–408 (1982).
- <sup>29</sup> Nemeč, N. & Cuniberti, G. Hofstadter butterflies of bilayer graphene. *Phys. Rev. B* 75,201404(R) (2007).
- <sup>30</sup> Bistritzer, R. & MacDonald, A. Moire butterflies in twisted bilayer graphene. *Phys. Rev.* B84, 035440(2011).
- <sup>31</sup> Moon, P. & Koshino, M. Energy spectrum and quantum Hall effect in twisted bilayer graphene. *Phys.Rev.* B85, 195458(2012).
- <sup>32</sup> R. Krishna Kumar, A. Mishchenko, X. Chen, S. Pezzini, G. H. Auton, L. A. Ponomarenko, U. Zeitler, L. Eaves, V. I. Fal'ko, and A. K. Geim, High-order fractal states in graphene superlattices. *PNAS* 115 (20) 5135-5139(2018).
- <sup>33</sup> J.O. Island, X. Cui, C. Lewandowski, J.Y. Khoo, E. M. Spanton, H. Zhou, D. Rhodes, J.C. Hone, T. Taniguchi, K. Watanabe, L.S. Levitov, M.P. Zaletel, A.F. Young, Spin-orbit driven band inversion in bilayer graphene by van der Waals proximity effect. *Nature* 571, 85–89 (2019).
- <sup>34</sup> Jairo Sinova, Dimitrie Culcer, Q. Niu, N. A. Sinitsyn, T. Jungwirth, and A. H. MacDonald, Universal intrinsic spin Hall effect. *Phys. Rev. Lett.* 92, 126603 (2004).
- <sup>35</sup> D. A. Abanin, S. V. Morozov, L. A. Ponomarenko, R. V. Gorbachev, A. S. Mayorov, M. I. Katsenelson, K. Watanabe, T. Taniguchi, K. S. Novoselov, L. S. Levitov, A. K. Geim; Giant Nonlocality Near the Dirac Point in Graphene, *Science* 15, 328-330(2011).
- <sup>36</sup> Y. K. Kato, R. C. Myers, A. C. Gossard, D. D. Awschalom, Observation of the spin Hall effect in semiconductors. *Science* 306, 1910 (2004)
- <sup>37</sup> Jayakumar Balakrishnan, Gavin Kok Wai Koon, Ahmet Avsar, Yuda Ho, Jong Hak Lee, Manu Jaiswal, Seung-Jae Baeck, Jong-Hyun Ahn, Aires Ferreira, Miguel A. Cazalilla, Antonio H. Castro Neto & Barbaros Özyilmaz; Giant spin Hall effect in graphene grown by chemical vapour deposition, *Nature Communications* 5, 4748 (2014)

- 
- <sup>38</sup> R. V. Gorbachev, J. C. W. Song, G. L. Yu, A. V. Kretinin, F. Withers, Y. Cao, A. Mishchenko, I. V. Grigorieva, K. S. Novoselov, L. S. Levitov, A. K. Geim, Detecting topological currents in graphene superlattices; *Science* 346, 448-451(2014).
- <sup>39</sup> Katsuyosih Komatsu, Yoshifumi Morita, Eiichiro Watanabe, Daiju Tsuya, Kenji Watanabe, Takashi Taniguchi and Satoshi Moriyama, Observation of the quantum valley Hall state in ballistic graphene superlattices, *Science Advances* 4, eaaq0194(2018).
- <sup>40</sup> Kaoru Kanayama and Kosuke Nagashio, Gap state analysis in electric-field-induced band gap for bilayer graphene. *Scientific Reports* 5, 15789 (2015).
- <sup>41</sup> Abanin, D. A., Shytov, A. V., Levitov, L. S. & Halperin, B. I. Nonlocal charge transport mediated by spin diffusion in the spin Hall effect regime. *Phys. Rev. B* 79, 035304 (2009).
- <sup>42</sup> Y. Shimazaki, M. Yamamoto, I. V. Borzenets, K. Watanabe, T. Taniguchi & S. Tarucha, Generation and detection of pure valley current by electrically induced Berry curvature in bilayer graphene. *Nature Physics* 11, 1032–1036(2015).
- <sup>43</sup> Jing Li, Ke Wang, Kenton J. McFaul, Zachary Zern, Yafei Ren, Kenji Watanabe, Takashi Taniguchi, Zhenhua Qiao and Jun Zhu, Gate-controlled topological conducting channels in bilayer graphene. *Nature Nanotechnology* 11, 1060–1065(2016).
- <sup>44</sup> M. A. M. Gijs and G. E.W. Bauer, Perpendicular giant magnetoresistance of magnetic multilayers *Adv. Phys.* 46, 285 (1997).
- <sup>45</sup> Daniel Loss and David P. DiVincenzo, Quantum computation with quantum dots. *Phys. Rev. A* 57, 120(1998).
- <sup>46</sup> L. Wang, I. Meric, P. Y. Huang, Q. Gao, Y. Gao, H. Tran, T. Taniguchi, K. Watanabe, L. M. Campos, D. A. Muller, J. Guo, P. Kim, J. Hone, K. L. Shepard, C. R. Dean, One-dimensional electrical contact to a two-dimensional material. *Science* 342, 614–617(2013).
- <sup>47</sup> A. V. Kretinin, Y. Cao, J. S. Tu, G. L. Yu, R. Jalil, K. S. Novoselov, S. J. Haigh, A. Gholinia, A. Mishchenko, M. Lozada, T. Georgiou, C. R. Woods, F. Withers, P. Blake, G. Eda, A. Wirsig, C. Hucho, K. Watanabe, T. Taniguchi, A. K. Geim, R. V. Gorbachev, Electronic properties of graphene encapsulated with different two-dimensional atomic crystals. *Nano Lett.* 14, 3270–3276 (2014).
- <sup>48</sup> F. Pizzocchero, L. Gammelgaard, B. S. Jessen, J. M. Caridad, L. Wang, J. Hone, P. Bøggild, T. J. Booth, The hot pick-up technique for batch assembly of van der Waals heterostructures. *Nat. Commun.* 7, 11894 (2016).
- <sup>49</sup> K. S. Novoselov, E. McCann, S. V. Morozov, V. I. Fal'ko, M. I. Katsnelson, U. Zeitler, D. Jiang, F. Schedin & A. K. Geim, Unconventional quantum Hall effect and Berry's phase of  $2\pi$  in bilayer graphene. *Nature Physics* 2, 177–180(2006).
- <sup>50</sup> R. T. Weitz, M. T. Allen, B. E. Feldman, J. Martin, A. Yacoby, Broken-Symmetry States in Doubly Gated Suspended Bilayer Graphene. *Science* 330, 812-812(2010).
- <sup>51</sup> Zhe Wang, Dong-Keun Ki, Jun Yong Khoo, Diego Mauro, Helmuth Berger, Leonid S. Levitov, and Alberto F. Morpurgo, Origin and Magnitude of 'Designer' Spin-Orbit Interaction in Graphene on Semiconducting Transition Metal Dichalcogenides. *PHYSICAL REVIEW X* 6, 041020 (2016).
- <sup>52</sup> A. Avsar, J. Y. Tan, T. Taychatanapat, J. Balakrishnan, G.K.W. Koon, Y. Yeo, J. Lahiri, A. Carvalho, A. S. Rodin, E.C.T. O'Farrell, G. Eda, A. H. Castro Neto & B. Özyilmaz, Spin-orbit proximity effect in graphene. *Nature Communications* 5, Article number: 4875 (2014).
- <sup>53</sup> Jose H. Garcia, Aron W. Cummings, and Stephan Roche, Spin Hall Effect and Weak Antilocalization in Graphene/Transition Metal Dichalcogenide Heterostructures. *Nano Lett.*, 8, 5078-5083(2017).
- <sup>54</sup> Martin Gmitra and Jaroslav Fabian, Proximity Effects in Bilayer Graphene on Monolayer WSe<sub>2</sub>: Field-Effect Spin Valley Locking, Spin-Orbit Valve, and Spin Transistor. *Phys. Rev. Lett.* 119, 146401 (2017).
- <sup>55</sup> Simon Zihlmann, Aron W. Cummings, Jose H. Garcia, Máté Kedves, Kenji Watanabe, Takashi Taniguchi, Christian Schönenberger, and Péter Makk Large spin relaxation anisotropy and valley-Zeeman spin-orbit coupling in **WSe<sub>2</sub>/graphene/h-BN** heterostructures, *Phys. Rev. B* 97, 075434(2018).

- 
- <sup>56</sup> A. W. Cummings, J. H. Garcia, J. Fabian, and S. Roche, *Giant Spin Lifetime Anisotropy in Graphene Induced by Proximity Effects*, Phys. Rev. Lett. **119**, 206601 (2017).
- <sup>57</sup> L. A. Benítez, J. F. Sierra, W. S. Torres, A. Arrighi, F. Bonell, M. V. Costache, and S. O. Valenzuela, *Strongly anisotropic spin relaxation in graphene/WS<sub>2</sub> van der Waals heterostructures*, Nature Physics **14**, 303–308(2018).
- <sup>58</sup> Edward McCann and Vladimir I. Fal'ko,  *$z \rightarrow -z$  Symmetry of Spin-Orbit Coupling and Weak Localization in Graphene*. Phys. Rev. Lett. **108**, 166606 (2012).
- <sup>59</sup> M. Büttiker, *Absence of backscattering in the quantum Hall effect in multiprobe conductors*. Phys. Rev. B **38**, 9375–9389 (1988).
- <sup>60</sup> Di Xiao, Ming-Che Chang, and Qian Niu, *Berry phase effects on electronic properties*. Rev. Mod. Phys. **82**, 1959(2010).
- <sup>61</sup> D. A. Abanin, S. V. Morozov, L. A. Ponomarenko, R. V. Gorbachev, A. S. Mayorov, M. I. Katsnelson, K. Watanabe, T. Taniguchi, K. S. Novoselov, L. S. Levitov, A. K. Geim, *Giant Nonlocality Near the Dirac Point in Graphene*. Science **332**, 328-330(2011).
- <sup>62</sup> R. V. Gorbachev, J. C. W. Song, G. L. Yu, A. V. Kretinin, F. Withers, Y. Cao, A. Mishchenko, I. V. Grigorieva, K. S. Novoselov, L. S. Levitov, A. K. Geim. *Detecting topological currents in graphene superlattices*. Science **346**, 448-451(2014).
- <sup>63</sup> D. A. Abanin, A. V. Shytov, L. S. Levitov, and B. I. Halperin, *Nonlocal charge transport mediated by spin diffusion in the spin Hall effect regime*. Phys. Rev. B **79**, 035304(2009).
- <sup>64</sup> Mikito Koshino and Tsuneya Ando, *Anomalous orbital magnetism in Dirac-electron systems: Role of pseudospin paramagnetism*. Phys. Rev. B **81**, 195431(2010).